HINS R&D Collaboration on Electron Cloud Effects: Midyear Report*

M. A. Furman,† K. Sonnad,‡ and J.-L. Vay§
Center for Beam Physics
Lawrence Berkeley National Laboratory, Bldg. 71R0259
1 Cyclotron Rd.
Berkeley, CA 94720
(Dated: Nov. 7, 2006)

We present a report on ongoing activities on electron-cloud R&D for the MI upgrade. These results update and extend those presented in Refs. 1, 2. In this report we have significantly expanded the parameter range explored in bunch intensity N_b, RMS bunch length σ_z and peak secondary emission yield (SEY) $\delta_{\max}$, but we have constrained our simulations to a field-free region. We describe the threshold behaviors in all of the above three parameters. For $\delta_{\max} \geq 1.5$ we find that, even for $N_b = 1 \times 10^{11}$, the electron cloud density, when averaged over the entire chamber, exceeds the beam neutralization level, but remains significantly below the local neutralization level (ie., when the electron density is computed in the neighborhood of the beam). This "excess" of electrons is accounted for by narrow regions of high concentration of electrons very close to the chamber surface, especially at the top and bottom of the chamber, akin to virtual cathodes. These virtual cathodes are kept in equilibrium, on average, by a competition between space-charge forces (including their images) and secondary emission, a mechanism that shares some features with the space-charge saturation of the current in a diode at high fields. For $N_b = 3 \times 10^{11}$ the electron cloud build-up growth rate and saturation density have a strong dependence on σ_z as σ_z decreases below ~ 0.4 m, when the average electron-wall impact energy roughly reaches the energy $E_{\max}$ where δ peaks. We also present improved results on emittance growth simulations of the beam obtained with the code WARP/POSINST in quasi-static mode, in which the beam-(electron cloud) interaction is lumped into N_s "stations" around the ring, where $N_s = 1, 2, \ldots, 9$. The emittance shows a rapid growth of $\sim 20\%$ during the first ~ 100 turns, followed by a much slower growth rate of $\sim 0.03\%$/turn. Concerning the electron cloud detection technique using microwave transmission, we present an improved dispersion relation for the TE mode of the microwaves, and a corresponding analytic estimate of the phase shift.

I. ELECTRON CLOUD BUILD-UP.

A. Remarks on the simulations.

We have replaced the Poisson solver of the code POSINST [3–6], used in the computation of the electron cloud space-charge forces, by a multigrid-type solver that is much faster and more accurate than the old one. We have carefully tested the new solver in stand-alone mode, and we are confident that it gives correct (indeed, quite accurate) results. Owing to its inefficiency, the old solver could realistically be used only for very coarse grids, leading to intermittent problems at high N_b and/or high $\delta_{\max}$ that sometimes crashed the code. For MI simulations, the improved code yields results only a few percent different from the old ones [1] for those cases in which the above-mentioned problem did not materialize. For other cases, notably the simulation of an LHC arc dipole, the improved code yields more benign results [7] for the electron-cloud density and power deposition than the old ones [8].

We have gone through the exercise of varying computational parameters (time step size, space-charge grid size, and maximum number of macroparticles allowed) to establish the conditions necessary for adequate numerical convergence. Parts of this exercise were carried out in the context of the LHC arc dipole electron cloud buildup simulations, and parts in the context of the MI simulations described here. Although we have not carried out the exercise for the complete range of values of the physical parameter explored, we have concluded that the space-charge grid for the MI needs to be 32×32 cells or denser to achieve reasonable numerical convergence for most of the cases explored. In practice, we have used a 64×64 grid for all cases; owing to the efficiency of the algorithm, this grid size does not lead to significantly more CPU time than a 32×32 grid. Fig. 1 shows a 64×64 grid superimposed on the MI chamber cross-section. We have also found that the average number of macroparticles needs to be not less than $\sim 5 - 10$ per grid cell when space-charge forces are important in order for the results to be smooth, a criterion we have adopted. Concerning the integration time step Δt, we have found that the cases with $\delta_{\max} \geq 1.5$ require smaller time steps, as described below.

*Work supported by the FNAL HINS R&D Effort and by the US DOE under contract DE-AC02-05CH11231.
†Electronic address: mafurman@lbl.gov; URL: http://mafurman.lbl.gov
‡Electronic address: kgsonnad@lbl.gov
§Electronic address: jlvay@lbl.gov

B. Assumptions on the SEY.

In this article we have also restricted our focus to only one model for the SEY, namely model "K" used in Ref. 1. This model was obtained from fits to measurements for stainless steel [5, 6], which originally showed $\delta_{\max} \simeq 2$ for the particular sample analyzed. Since we are interested here in exploring the sensitivity to $\delta_{\max}$, we have simply scaled the curve $\delta(E_0)$ by a constant factor, where E_0 is the incident electron energy. In this way the energy $E_{\max}$ at which $\delta(E_0)$ peaks, $\delta_{\max} \equiv \delta(E_{\max})$, remains unchanged, while the 0-energy value of the SEY, $\delta(0)$, scales linearly with $\delta_{\max}$. Fig. 2 shows the SEY curve for the case $\delta_{\max} = 1.7$ and $E_{\max} = 293$ eV.

While our simple scaling prescription does not quite correspond to the physical process of conditioning, which slightly shifts $E_{\max}$ and does not maintain the proportionality $\delta(0) \propto \delta_{\max}$, it allows us to conveniently explore parameter space over a broad range. We intend to carry out more detailed and faithful simulations, including conditioning effects, after at least a few benchmarks against MI measurements.

C. Parameter range explored.

In all build-up simulations presented here we consider only a field-free region of the MI at injection energy, $E_b = 8.9$ GeV. The three main parameters varied here are N_b, σ_z, and $\delta_{\max}$.

We have significantly expanded the range of parameters explored relative to [1]. Specifically, in this report we consider the following values for N_b, σ_z, and $\delta_{\max}$:

- $N_b = (0.6, 1, 1.5, 2, 3) \times 10^{11}$
- $\sigma_z = 0.1, 0.15, 0.2, 0.25, 0.3, 0.4, 0.5, 0.6, 0.75$ m
- $\delta_{\max} = 1.1, 1.2, 1.3, 1.4, 1.5, 1.7$

but not in all combinations. In addition, in all cases studied, we have assumed a transverse RMS beam size $\sigma_{\rm tr} = 5$ mm, as in Ref. 1; however, we have tested the sensitivity of the results for high $\delta_{\max}$ by also setting $\sigma_{\rm tr} = 1$ mm ($\sigma_{\rm tr} \equiv \sigma_x = \sigma_y$). Other parameters used to obtain the present results are the same as those listed in Ref. 1, except that now we have:

1. used the new multigrid Poisson solver with a grid of 64×64 cells instead of the old solver with a grid of 26×10 cells;
2. used the correct injection beam energy $E_b = 8.9$ GeV instead of 8 GeV;
3. used 10 times more primary macroelectrons per bunch passage than before (input parameters `macroionel=90`, `macroplel=10` rather than `macroionel=9`, `macroplel=1`);
4. Set a limit of 20000 for the maximum number of macroelectrons allowed in the simulation at any given time instead of 2000 (input parameter `nexmax`);
5. used typically only two booster batches (168 bunches) instead of 6 to save on CPU time (however, all average quantities shown in Figs. 3-12 were computed in steady state, typically reached well before the end of the 2nd batch). We have spot-checked with six booster batches (504 bunches) in a few marginal cases;
6. used much smaller integration time steps for the higher values of $\delta_{\max}$, namely 67 kicks per bunch length and 122 kicks per inter-bunch gap instead of 11 and 9 for the other cases presented here (input parameters `nkicks` and `nsteps`, respectively).

Table I summarizes the parameters used here, and defines many other variables.

D. Bunch-length dependence.

As we made progress in our simulations and gradually learned to adjust the numerical integration parameters, we ended up with two sets of simulations:

1. Higher-$\delta_{\max}$ set: $\delta_{\max} = 1.3$, 1.5 and 1.7, $N_b = 1 \times 10^{11}$, and $(N_k, N_g) = (67, 122)$.
2. Lower-$\delta_{\max}$ set: $\delta_{\max} = 1.1$, 1.2, 1.3 and 1.4, $N_b = (6 - 30) \times 10^{10}$, $(N_k, N_g) = (11, 9)$.

In both sets we varied σ_z but not for all possible combinations of the other parameters.

1. *Results for the higher-δ_{max} set.*

Build-up results for $\delta_{\max} = 1.3$ or 1.7, and $\sigma_z = 0.75$ m or 0.1 m, are shown in Fig. 3, which shows the average electron cloud line-charge density $\lambda_e(t)$. A strong dependence on σ_z is evident. For $\delta_{\max} = 1.3$ and $\sigma_z = 0.75$ m there is no significant electron cloud build-up (no multipacting mechanism), resulting in a low-density saturation. For the other cases there is a clear exponential growth of the electron density during the first ~ 1.5 μs, with a growth rate and saturation level strongly dependent on σ_z.

The two bottom plots of Fig. 3, corresponding to $\delta_{\max} = 1.7$, show that the average electron cloud density exceeds the average beam neutralization level by factors 2–3 in steady state. This phenomenon can be examined in more detail by looking at the time-averaged xy projection of the electron density, shown in Fig. 4. The four plots here correspond directly to the same cases shown in Fig. 3. It is clear that, when an exponential growth takes

TABLE I: Assumed MI parameters for EC simulations.

Parameter	Symbol (unit)	Value
Ring and beam parameters		
Ring circumference	C (m)	3319.419
Beam energy	E_b (GeV)	8.9
Relativistic beam factor	γ_b	9.4855
Revolution period	T_0 (μs)	11.134
Beam pipe cross section	$\cdots$	elliptical
Beam pipe semi-axes	(a, b) (cm)	(6.15,2.45)
Harmonic number	h	588
RF wavelength	$\lambda_{\rm RF}$ (m)	5.645270
No. bunches per beam	$\cdots$	168 or 504
Bunch spacing	s_b (m)	5.645270
Gap length	$\cdots$ (buckets)	84
Bunch population	N_b	$(0.6-3)\times10^{11}$
RMS bunch length	σ_z (m)	0.1–0.75
Longit. bunch profile	$\cdots$	gaussian
Transverse bunch profile	$\cdots$	gaussian
Average beta function	$\bar{\beta}$ (m)	25
Normalized tr. emittance (95%)	ϵ_N (m-rad)	40π
RMS relative momentum spread	σ_p/p	10^{-3}
Transverse RMS bunch sizes	(σ_x, σ_y) (mm)	(1,1) or (5,5)
Primary e$^-$ parameters		
Proton loss rate	n'_{pl} (p/m)	1×10^{-10}
Proton-electron yield	$\eta_{\rm eff}$	100
Residual gas pressure	P (nTorr)	20
Temperature	T (K)	305
Ionization cross-section	σ_i (Mbarns)	2
Proton-loss e$^-$ creation rate	$n'_{e(pl)}$ ((e/p)/m)	1×10^{-8}
Ionization e$^-$ creation rate	$n'_{e(i)}$ ((e/p)/m)	1.27×10^{-7}
Secondary e$^-$ parameters		
Peak SEY	$\delta_{\rm max}\equiv\delta(E_{\rm max})$	1.1–1.7
Energy at peak SEY	$E_{\rm max}$ (eV)	293
SEY at 0 energy	$\delta(0)$	$0.2438\times\delta_{\rm max}$
Backscattered component at $E_{\rm max}$	$\delta_e(E_{\rm max})+\delta_r(E_{\rm max})$	$0.406\times\delta_{\rm max}$
Simulation parameters		
Simulated section	$\cdots$	field-free region
Length of simulated region	L (m)	0.1
No. kicks/bunch	N_k	11 or 67
(Full bunch length)/(RMS bunch length)	L_b/σ_z	4
No. steps between bunches	N_g	9 or 122
No. primary macroelectrons/bunch	M_e	100
Max. no. of macroelectrons allowed	$\cdots$	20000
Space-charge grid size	$\cdots$	64×64
Time step size	Δt (ns)	0.02–1

place (bottom 3 cases), the electron cloud density develops small regions of high concentration very near the chamber, predominantly at the top and bottom, while the density near the beam remains at a much lower level. Simulated digital movies in similar cases show that these regions of high electron density near the walls are kept stable by a competition between the space-charge forces (including the image forces), and secondary emission. In effect, a local minimum of the potential develops inside the chamber near the walls, leading to these so-called "virtual cathodes." This mechanism is somewhat similar to the space-charge saturation of the current in a diode at high fields [9]. We are not certain that our simulation yields quantitatively correct results for the virtual cathode density, and we have not explored this issue in any further detail. One reason we hesitate over the quantitative validity of the virtual cathodes is that the SEY in our secondary emission model is wholly independent of the space-charge fields acting upon the surface. On the other hand, basic physical arguments would seem to indicate a suppression effect of the SEY which would diminish the virtual cathode effect. We have not attempted to determine the magnitude of this suppression. It seems to us that further investigation of this issue is desirable.

Fig. 5 shows the steady-state averages of the electron cloud volumetric density as a function of σ_z for $N_b = 1\times10^{11}$ and $\delta_{\max} = 1.3$, 1.5 and 1.7. As mentioned above, the average electron cloud density exceeds the saturation level for $\delta_{\max} \geq 1.5$ (top plot), but the electron density within the 1σ beam ellipse, although somewhat higher than the overall average, is nevertheless far below the *local* neutralization level (bottom plot). In addition, Fig. 5 shows that the overall electron density is fairly insensitive to transverse beam size $\sigma_{\rm tr}$, but the local density near the beam does show some sensitivity.

Fig. 6 shows, for the same conditions as in the above figures, the σ_z dependence of the electron flux at the wall, average electron cloud energy, and average electron-wall impact energy. It is apparent that all these quantities increase as σ_z decreases, and none of them show a strong sensitivity to $\sigma_{\rm tr}$. It is worth noting that the average electron-wall impact energy remains well below $E_{\max} =$ 293 eV even at the lowest value of σ_z explored, $\sigma_z = 0.1$ m.

Finally, Fig. 7 shows the detailed evolution of the electron cloud during the passage of two consecutive bunches, for a total time interval of 35 ns, for $N_b = 1\times10^{11}$ and $\delta_{\max} = 1.7$. The specific time interval shown here, centered about $t = 2$ μs, is well within the steady-state regime of the electron cloud build-up (see Fig. 3). It is apparent that the overall electron cloud density does not fluctuate much in time, but the local electron density (within the 1σ beam ellipse) fluctuates quite strongly, with strong sensitivity to σ_z. The electron density at the bunch center is significantly higher for $\sigma_z = 0.75$ m ($d \simeq 3\times10^{13}$ m^{-3}) than for $\sigma_z = 0.1$ m ($d \simeq 1\times10^{13}$ m^{-3}). This implies a larger neutralization tune shift for the longer-bunch case, and higher potential for instability, than for the shorter-bunch case.

The space-charge neutralization tune shift per unit length, $\Delta\nu/L$, is given by [10]

$$\Delta\nu/L = \frac{r_p\bar{\beta}d}{2\gamma_b} \tag{1}$$

where $r_p = 1.535\times10^{-18}$ m is the classical proton radius. Setting $d = 1\times10^{13}$ m^{-3} we obtain

$$\Delta\nu/L = 2\times10^{-5} \quad \text{m}^{-1} \tag{2}$$

To get a rough idea of the overall magnitude of $\Delta\nu$, we may substitute C for L, yielding $\Delta\nu \simeq 0.07$ for the total tune shift. For the $\sigma_z = 0.75$-m case, the estimate of $\Delta\nu$ is $\sim$3 times larger.

2. Results for the lower-δ_{max} set.

Fig. 8 shows the build-up of the electron cloud for $\delta_{\max} = 1.1 - 1.4$, $N_b = (6-30)\times10^{10}$, and $\sigma_z = 0.75$ m, specifically the average beam neutralization factor $\chi(t) = \lambda_e(t)/\bar{\lambda}_b$, where $\bar{\lambda}_b = eN_b/s_b$. It is apparent that an exponential growth of the cloud does not occur unless N_b or $\delta_{\max}$ are sufficiently high, implying a threshold behavior in either of these two variables.

If N_b is fixed at 3×10^{11}, Fig. 9 shows the σ_z-dependence of the average electron cloud density and the 1σ density. In contrast with the $N_b = 1\times10^{11}$ case (Fig. 5), the average density now decreases when σ_z decreases. This qualitatively different behavior is almost certainly due to the fact that, as σ_z decreases, the average electron-wall impact energy crosses $E_{\max}$, hence the effective SEY peaks in the mid-range of σ_z, as seen in Fig. 10 (bottom).

E. Bunch-intensity dependence.

Figs. 11 and 12 summarize the dependence of various quantities, averaged in steady state, on N_b for the lower-$\delta_{\max}$ set. In these cases we have fixed $\sigma_z = 0.75$ m. As already stated in Sec. I D 2, the electron cloud density and flux at the wall exhibit a threshold behavior in N_b, and the threshold value of N_b depends strongly on $\delta_{\max}$. On the other hand, the average electron energy, is a smooth function of N_b, as it should be expected.

F. Transverse bunch-size dependence.

As explained inf Sec. I D 1, we have only tested the dependence on $\sigma_{\rm tr}$ for a subset of the higher-$\delta_{\max}$ set, specifically for $\delta_{\max} = 1.7$ and $N_b = 1\times10^{11}$. For this case, we have compared results for $\sigma_{\rm tr} = 5$ mm vs. $\sigma_{\rm tr} = 1$ mm. As seen in Figs. 5 and 6, the only average quantity that shows some significant sensitivity to $\sigma_{\rm tr}$ is the 1σ

electron density. Although a smaller $\sigma_{\rm tr}$ leads in principle to stronger beam-electron kicks, there are relatively very few electrons (only those close to the edge of the beam) that experience them, hence the quantities averaged over the entire electron cloud are not expected to be very sensitive to $\sigma_{\rm tr}$ for typical conditions. On the other hand, local quantities (pertaining to electrons close to the beam), are naturally expected to be sensitive to $\sigma_{\rm tr}$.

II. ELECTRON CLOUD EFFECTS ON THE BEAM.

We have implemented a quasi-static mode (QSM) of operation in the 3D self-consistent code WARP/POSINST. The QSM affords much faster simulations than the fully self-consistent 3D mode. In the QSM approximation, a given bunch in the beam, represented by macroprotons, interacts with an initially-uniform 2D electron cloud at a number N_s of discrete locations (called "stations") around the ring. During the passage of the bunch through the electron cloud, the beam particles and the electrons move in response to each other under their mutual influence. The electron cloud at each station is refreshed before the next bunch passage. After a bunch passes through a station, it is transported to the next station by means of a lattice map (a map capability has also been recently implemented in WARP/POSINST), or by leap-frog integration of the equations of motion for the protons. The intensity of the lumped electron cloud is inversely proportional to N_s, so the aggregate intensity around the ring corresponds to the physical case. The physical limit corresponds to $N_s \to \infty$. We have benchmarked WARP/POSINST in QSM against the CERN code HEADTAIL for the case of the LHC beam, showing excellent agreement [11, 12].

Fig. 13 shows the beam emittance evolution for ∼600 turns, for $N_s = 1, 2, \ldots, 9$, of a bunch with $N_b = 3\times10^{11}$ and $\sigma_z = 0.75$ m, and assuming an electron cloud density of 1×10^{12} m^{-3}. It is apparent that the vertical emittance has nicely converged already at $N_s = 3$, but the horizontal emittance seems to require $N_s > 9$ for sensible convergence. We do not have an explanation for this difference in the convergence rate. However, after a rapid inital emittance growth (probably due to a mismatch in the initial conditions of the bunch and electron cloud distributions), the emittance growth rate stabilizes to $\sim 0.03\%$/turn.

III. MICROWAVE PROPAGATION THROUGH THE ELECTRON CLOUD.

A technique to measure the average electron cloud density in a section of a storage ring non-destructively, parasitically, and in real time, has been devised by Caspers and Kroyer, and tested at the SPS [13–15]. The technique consists in injecting microwaves into the vacuum chamber and detecting their phase shift and attenuation a distance ΔL away. The electron cloud density can be inferred from these measurements if a theoretical or simulation analysis is available for the phase shift and attenuation. For typical operating conditions, the beam itself leads to a relatively small (and calculable) perturbation on these quantities owing to the significantly different frequency spectrum than the electron cloud.

We have computed an improved expression for the phase shift expected in a uniform electron cloud. The dispersion relation for the TE mode of an EM wave of wavenumber k and angular frequency ω propagating in a cylindrical pipe of radius R containing a plasma of frequency ω_p is given by [16]

$$\omega^2 - (ck)^2 - \omega_p^2 = \omega_c^2 \tag{3}$$

where $\omega_c \equiv c\alpha_{\ell n}/R$ is the cutoff frequency, $\alpha_{\ell n}$ being the nth root of the derivative of the Bessel function of order ℓ, $J'_\ell(x)$. The phase shift over a distance ΔL arising from the presence of the plasma is $\Delta\phi = (k_v - k)\Delta L$ where k_v is the wave number in vacuum under similar conditions. Thus

$$\Delta\phi = \left[(\omega^2 - \omega_c^2)^{1/2} - (\omega^2 - \omega_c^2 - \omega_p^2)^{1/2}\right]\frac{\Delta L}{c} \tag{4}$$

The plasma frequency $\omega_p = \sqrt{e^2 d/(\epsilon_0 m_e)} = c\sqrt{4\pi r_e d}$ is 56.4 MHz for an electron cloud density $d = 1\times10^{12}$ m^{-3} (here m_e and r_e are the mass and classical radius of the electron, respectively). If we assume $R = 5$ cm and a mode corresponding to $(\ell, n) = (1, 2)$, we obtain $\omega_c = 18.3$ GHz. In the approximation $\omega \gg \omega_p$, which is typical, the above reduces to

$$\Delta\phi = \frac{\omega_p^2\,\Delta L}{2c(\omega^2 - \omega_c^2)^{1/2}} \tag{5}$$

This expression reduces to that given by T. Kroyer and F. Caspers [13–15] for wave propagation in the absence of a pipe ($\omega_c = 0$).

IV. CONCLUSIONS AND FUTURE WORK.

We now have a better quantitative description of the sensitivity of the electron cloud for field-free regions in the MI to the three main parameters N_b, σ_z and $\delta_{\rm max}$. Threshold behaviors are observed in this 3D parameter space. The determination of a "phase diagram" in this space is possible from our current results, but smooth, well-demarcated boundaries would require more, finer, simulations. A natural criterion used to define the phase diagram would be based upon the exponential growth rate of the electron cloud build-up.

Recent measurements of the SEY of MI chamber samples indicate $\delta_{\rm max} \simeq 2$ and $E_{\rm max} \simeq 350$ eV [17]. In our simulations we have so far constrained $\delta_{\rm max}$ not exceed 1.7, and we have fixed $E_{\rm max} = 293$ eV. Even for

$\delta_{\max} = 1.7$ our electron cloud simulations indicate a rather strong effect on the average density. It appears at first sight that our simulations indicate a stronger electron cloud effect than what is observed at the MI. It seems to us that a benchmarking exercise, in which our simulations for the electron cloud buildup and electron flux is methodically compared against in-situ measurements at the MI, should have high priority. Such a benchmark would tell us which parameters need adjusting in order to achieve faithful results and predictions. The parameters $E_{\max}$ and $\delta(0)$, which we have not yet exercised independently, are likely to be relevant. Furthermore, we do not yet have a good quantitative description of the electron cloud effects on the beam, especially instabilities, which would afford an ultimate benchmark against observations.

The effect of the beam energy E_b on the electron cloud is essentially indirect: given N_b, σ_x, σ_y and σ_z, the electron cloud is essentially determined without further reference to E_b. The only other way in which E_b enters is through the bunch spacing in time and the longitudinal field produced by the bunch, but such effects are weak as long as the beam is sufficiently relativistic, which is typically the case. On the other hand, the effcets from the electron cloud on the beam are sensitive to E_b. For example, the space-charge neutralization tune shift is explicitly proportional to E_b^{-1}. Such dependence is typical of conventional impedance effects.

Our results indicate strong sensitivities of global electron cloud quantities to N_b, σ_z and $\delta_{\max}$ but not to $\sigma_{\rm tr}$. Local quantities (ie., close to the beam center) are sensitive to $\sigma_{\rm tr}$. While these sensitivities can be understood from basic physical considerations, there are unresolved details such as:

- For $N_b = 3 \times 10^{11}$, why is it that the density and e-wall flux peak at $\sigma_z \sim 0.4$ m? The simple expectation is that this should happen at $\sigma_z \sim 0.25$ m, since the average electron-wall impact energy reaches a value $= E_{\max}$ at this value of σ_z.

- To what extent are the virtual cathodes described in Sec. I D 1 real? The physical mechanism that gives rise to them are well understood, but we are uncertain as to the quantitative aspects. An intriguing question we would like to answer is the extent to which the SEY is suppressed by space-charge forces. Even a relatively small suppression would probably lead to more benign electron cloud effects in general, and to weaker virtual cathodes.

- Why do the simulations of the horizontal and vertical emittance growth rates show a qualitative difference in convergence rate?

It is possible that the inherently 2D nature of the code POSINST leads to stronger-than-real electron cloud effects, including the average electron density, especially for field-free regions. In reality, the electrons would probably be pushed longitudinally by the space-charge forces, presumably leading to a smaller density. Such forces are absent in POSINST. For other regions, such as dipole fields, the space-charge longitudinal forces are typically ineffective against the B-field trapping mechanism, hence the 2D approximation is easier to justify in these cases. A simple code-to-code benchmark to test the degree of validity of the 2D POSINST approximation would be to carry out a 3D electron cloud build-up simulations with WARP/POSINST using frozen (non-dynamical) beams, as in POSINST. Such a simulation would require minimal extra code development on WARP/POSINST.

Future activities we intend to carry out include:

1. Carry out further build-up simulations with parameters resembling as close as possible those relevant to the MI measurement setup [18], and the SEY measurements of chamber samples [17].

2. Extend our build-up simulations to dipole magnetic fields to explore any potential qualitatively different behaviors (which we do not expect, but which should be checked).

3. Continue and augment WARP/POSINST simulations to study the effects of the electron cloud on the beam, with special attention to potential instabilities.

4. Apply WARP/POSINST to simulate the electron cloud build-up in 3D with non-dynamical beams, as a way to benchmark the 2D calculations carried out with POSINST.

5. Continue to refine the analysis of the microwave transmission through the electron cloud, eg., by taking into account effects from electron cloud temperature and non-uniformities, presence of the beam, etc., to the extent that is analytically possible.

6. Evaluate the application of an EM code such as VORPAL to simulate microwave transmission through the electron cloud for more realistic conditions.

7. If possible, participate, or at least be in the loop, in forthcoming measurements of the microwave transmission technique at PEP-II.

Acknowledgments

We are deeply grateful to J. Qiang for providing us with a multigrid Poisson solver. We are indebted to R. Zwaska for discussions and guidance on our work. We are grateful to NERSC for supercomputer support.

[1] M. A. Furman, "A preliminary assessment of the electron cloud effect for the FNAL main injector upgrade," LBNL-57634/CBP-Note-712/FERMILAB-PUB-05-258-AD, 23 June 2006.

[2] M. A. Furman, "HINS R&D Collaboration on Electron Cloud Effects: Midyear Progress Report," CBP-Technote-364, 22 Sept. 2006.

[3] M. A. Furman and G. R. Lambertson, "The electron-cloud instability in the arcs of the PEP-II positron ring," LBNL-41123/CBP Note-246, PEP-II AP Note AP 97.27 (Nov. 25, 1997). Proc. *Intl. Workshop on Multibunch Instabilities in Future Electron and Positron Accelerators "MBI-97"* (KEK, 15-18 July 1997; Y. H. Chin, ed.), KEK Proceedings **97-17**, Dec. 1997, p. 170.

[4] M. A. Furman, "The electron-cloud effect in the arcs of the LHC," LBNL-41482/CBP Note 247/LHC Project Report 180 (May 20, 1998).

[5] M. A. Furman and M. T. F. Pivi, "Probabilistic model for the simulation of secondary electron emission," LBNL-49771/CBP Note-415 (Nov. 6, 2002). PRST-AB **5** 124404 (2003), http://prst-ab.aps.org/pdf/PRSTAB/v5/i12/e124404.

[6] M. A. Furman and M. T. F. Pivi, "Simulation of secondary electron emission based on a phenomenological probabilistic model," LBNL-52807/SLAC-PUB-9912 (June 2, 2003).

[7] M. A. Furman, "ECLOUD in PS2, PS+, SPS+," LBNL-61925, CBP Note 762, Nov. 7, 2006; Proc. LHC LUMI 2006 CARE-HHH-APD Workshop "Towards a Roadmap for the Upgrade of the CERN and GSI Accelerator Complex," IFIC (Valencia, Spain), 16–20 October 2006, http://care-hhh.web.cern.ch/CARE-HHH/LUMI-06/default.html

[8] M. A. Furman and V. H. Chaplin, "Update on electron-cloud power deposition for the LHC arc dipoles," LBNL-59062/CBP Note 723, January 30, 2006; PRST-AB 9, 034403 (2006). http://prst-ab.aps.org/pdf/PRSTAB/v9/i3/e034403

[9] See, eg., A. van der Ziel, *Solid State Physical Electronics*, Prentice-Hall, 1976 (3rd. ed.), ch. 7.

[10] M. A. Furman and A. Zholents, "Incoherent Effects Driven by the Electron Cloud," LBNL-42688, CBP Note 286, March 29, 1999. Proc. PAC99 (New York City, March 29-April 2, 1999), p. 1794 (paper TUP130).

[11] J.-L. Vay, M. A. Furman, P. A. Seidl, R. H. Cohen, A. Friedman, D. P. Grote, M. Kireeff-Covo, A. W. Molvik, P. H. Stoltz, S. Veitzer, J. P. Verboncoeur, "New simulation capabilities of electron clouds in ion beams with large tune depression," HIFAN 1460, LBNL-60636; 39th ICFA Advanced Beam Dynamics Workshop on High Intensity High Brightness Hadron Beams "HB2006," Epochal International Congress Center, Tsukuba, Japan, May 29-June 2, 2006.

[12] J. L. Vay, M. Furman, R. Cohen, A. Friedman, D. Grote, A. Molvik, P. Stoltz, S. Veitzer, J. Verboncoeur, "Filling in the Roadmap for Self-Consistent Electron Cloud and Gas Modeling," HIFAN 1385, LBNL-56869. Proc. PAC05, Knoxville, TN, May 16-22nd, 2005.

[13] T. Kroyer, F. Caspers, W. Höfle, J. M. Jiménez, J.-F. Malo, J. Tückmantel, "Unexpected Results on Microwave Waveguide Mode Transmission Measurements in the SPS Beam Pipe," Proc. ECLOUD04.

[14] T. Kroyer, "Application of Waveguide Mode Diagnostics for Remote Sensing in Accelerator Beam Pipes," Ph.D. dissertation, May 2005. Institut für Nachrichtentechnik und Hochfrequenztechnik eingereicht an der Technischen Universität Wien, Fakultät für Elektrotechnik und Informationstechnik.

[15] T. Kroyer, F. Caspers, E. Mahner, "The CERN SPS Experiment on Microwave Transmission Through the Beam Pipe," Proc. PAC05, paper MPPP031.

[16] H. S. Uhm, K. T. Nguyen, R. F. Schneider and J. R. Smith, "Wave dispersion theory in a plasma column bounded by a cylindrical waveguide," J. Appl. Phys. **64**(3), 1108 (1 Aug. 1988).

[17] R. Kirby, "SLAC SEY and Surface Analysis Measurements on FNAL Main Injector Ring S/S Beam Chamber Material," Sept. 5, 2006.

[18] R. Zwaska, "Early slides," PPT file, Sept. 2006.

DISCLAIMER

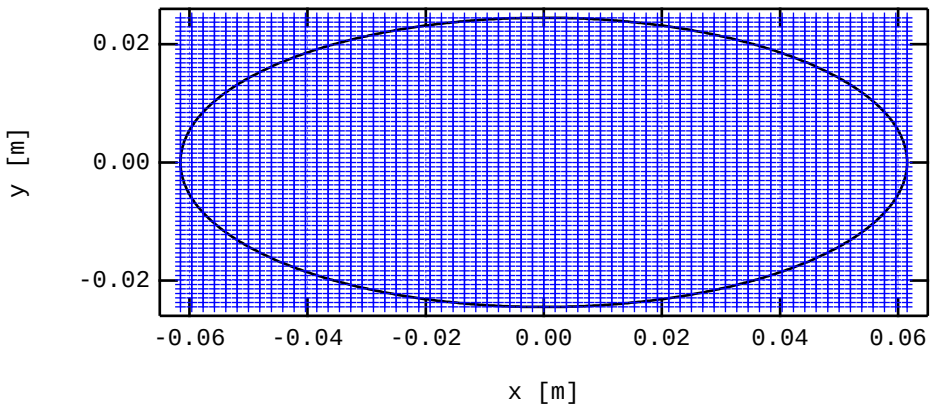

FIG. 1: MI chamber cross-section and the grid used to compute the space-charge forces. The grid is of size 64×64 cells, so that the number of cells within the elliptical chamber is $\simeq 3216$.

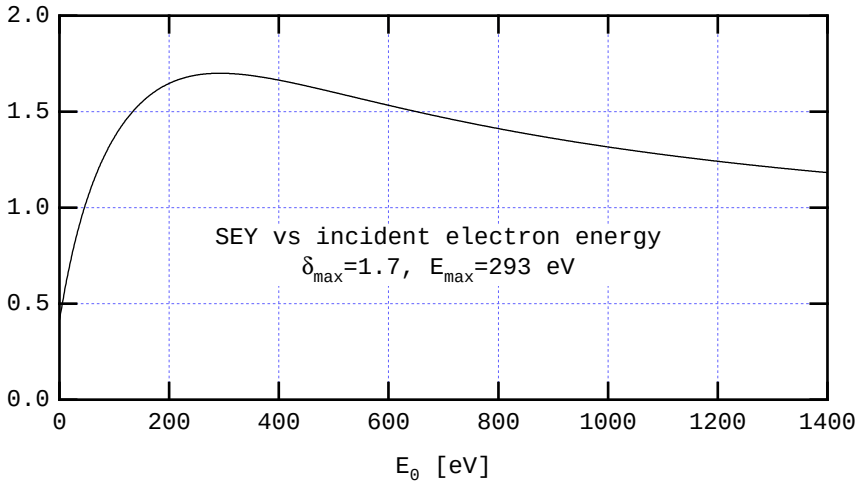

FIG. 2: Sample SEY curve used in the simulations. This particular case has a peak value $\delta(E_{\max}) \equiv \delta_{\max} = 1.7$ and $\delta(0) = 0.414$. For other values of $\delta_{\max}$, we simply scale this curve by a constant factor. The location of the peak, $E_{\max} = 293$ eV, is unchanged by this scaling. Obtained by scaling a fit to measured data for stainless steel [5, 6].

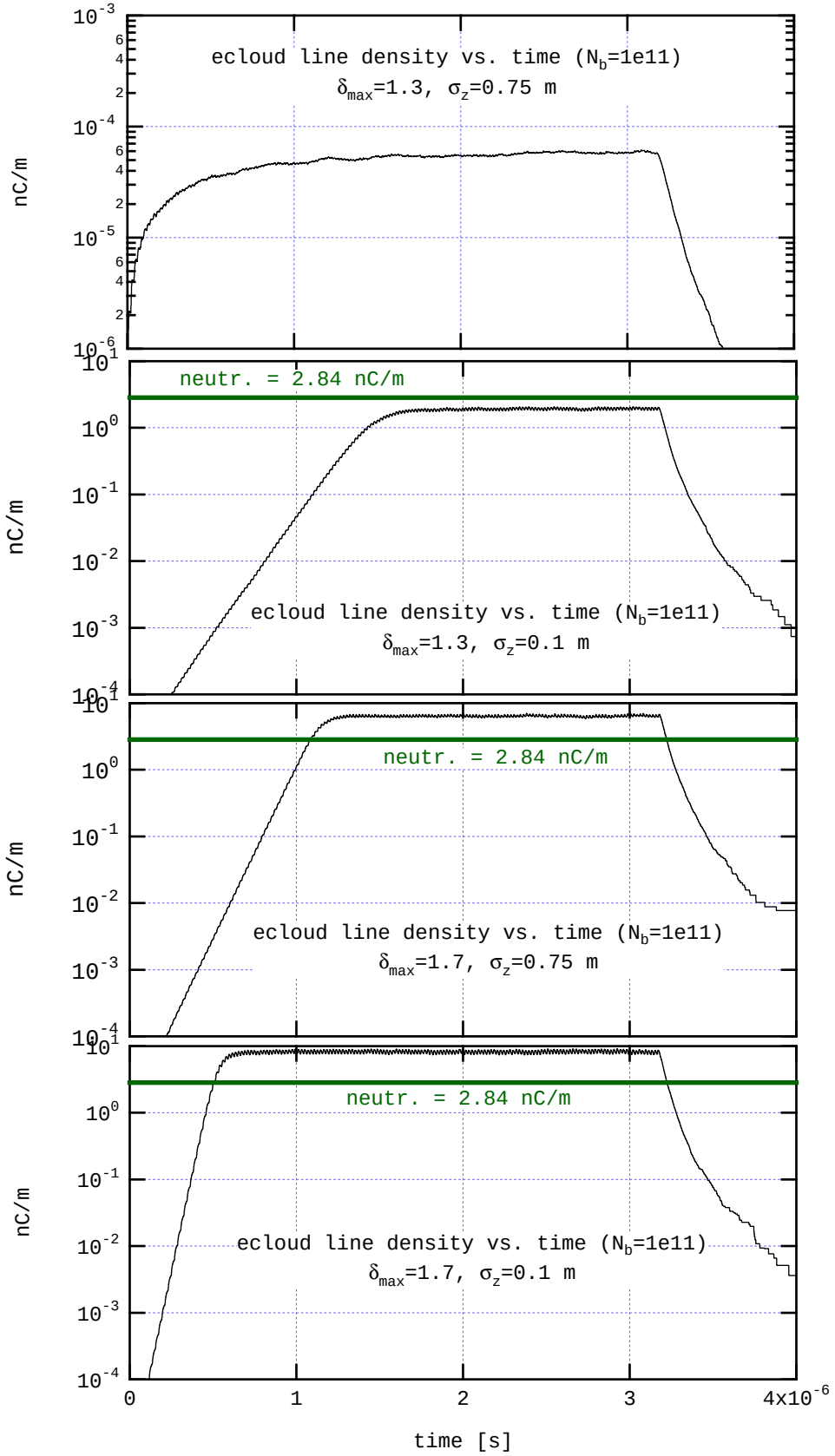

FIG. 3: Build-up of the average electron-cloud line density for $N_b = 1 \times 10^{11}$ for a beam consisting of two booster batches (168 bunches). The top two cases correspond to $\delta_{\max} = 1.3$, while the bottom two to $\delta_{\max} = 1.7$. For each value of $\delta_{\max}$ we consider σ_z either 75 cm or 10 cm. The strong dependence of the growth time and the saturation level on σ_z is evident. The beam neutralization level ("neutr.") of the electron-cloud line density is given by $\bar{\lambda}_b = eN_b/s_b = 2.84$ nC/m. Although the average electron-cloud density exceeds the beam neutralization level for $\delta_{\max} = 1.7$, the *local* density near the beam is significantly below neutralization (see Fig. 5). In these cases the electron distribution develops small regions of high density at the top and bottom of the chamber (see Fig. 4 for the xy projection of the density for the cases above).

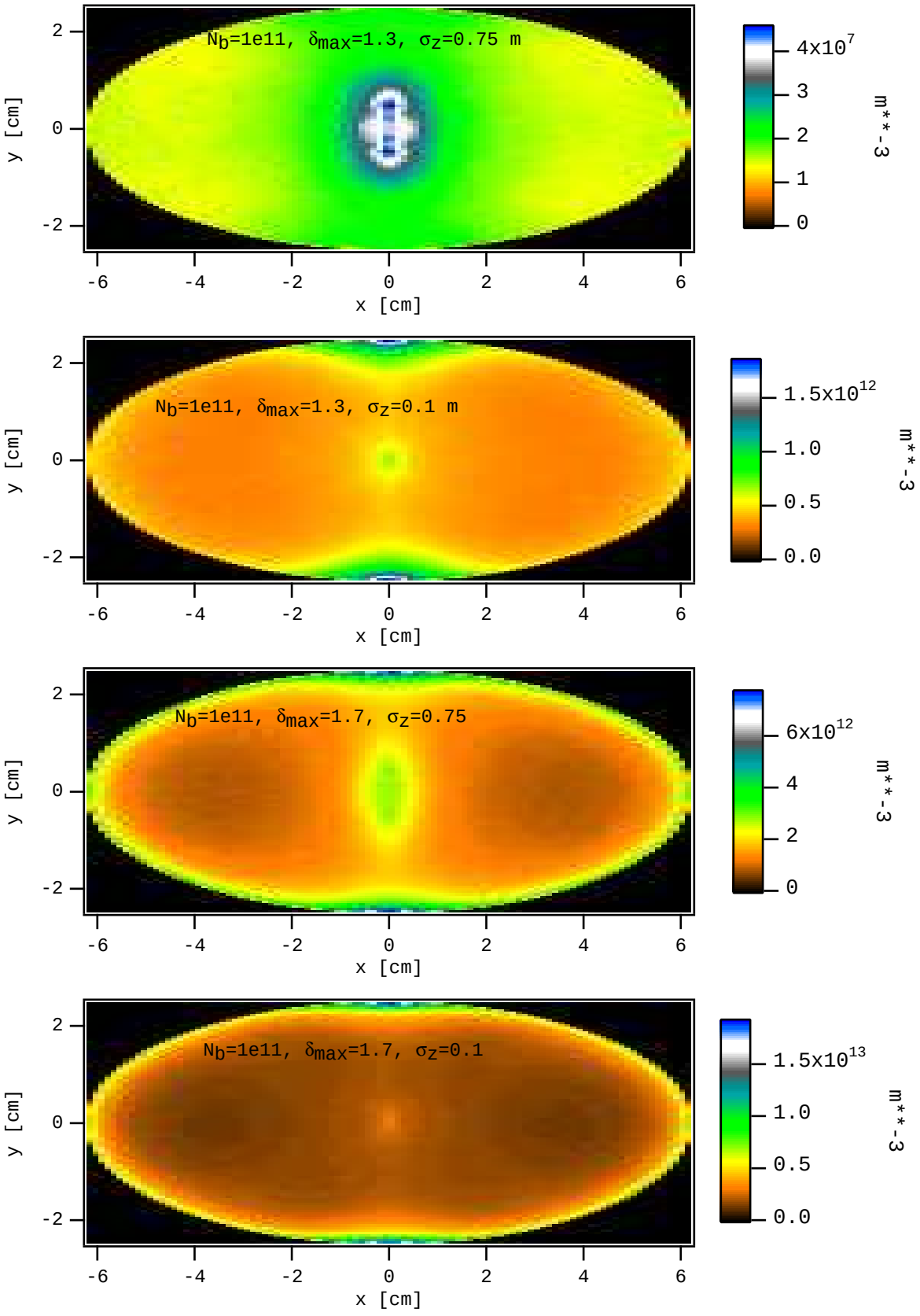

FIG. 4: Time-average of the xy projection of the electron-cloud density. For the top two plots $\delta_{\max}$ was assumed to be 1.3, while the RMS bunch length σ_z was either 75 cm or 10 cm. Bottom two plots: same, except $\delta_{\max} = 1.7$. Bunch intensity was $N_b = 1 \times 10^{11}$ in all cases. The average over time was taken over one full revolution of the MI ($T_0 = 11.1$ μs), but the beam consisted of only two booster batches (168 bunches), lasting only ~ 3.2 μs. For all cases except the top, the electron-cloud builds up exponentially in time (see Fig. 3), reaching a saturation within $\sim$1–2 μs. In these cases regions of high local electron density develop at the top and bottom of the chamber.

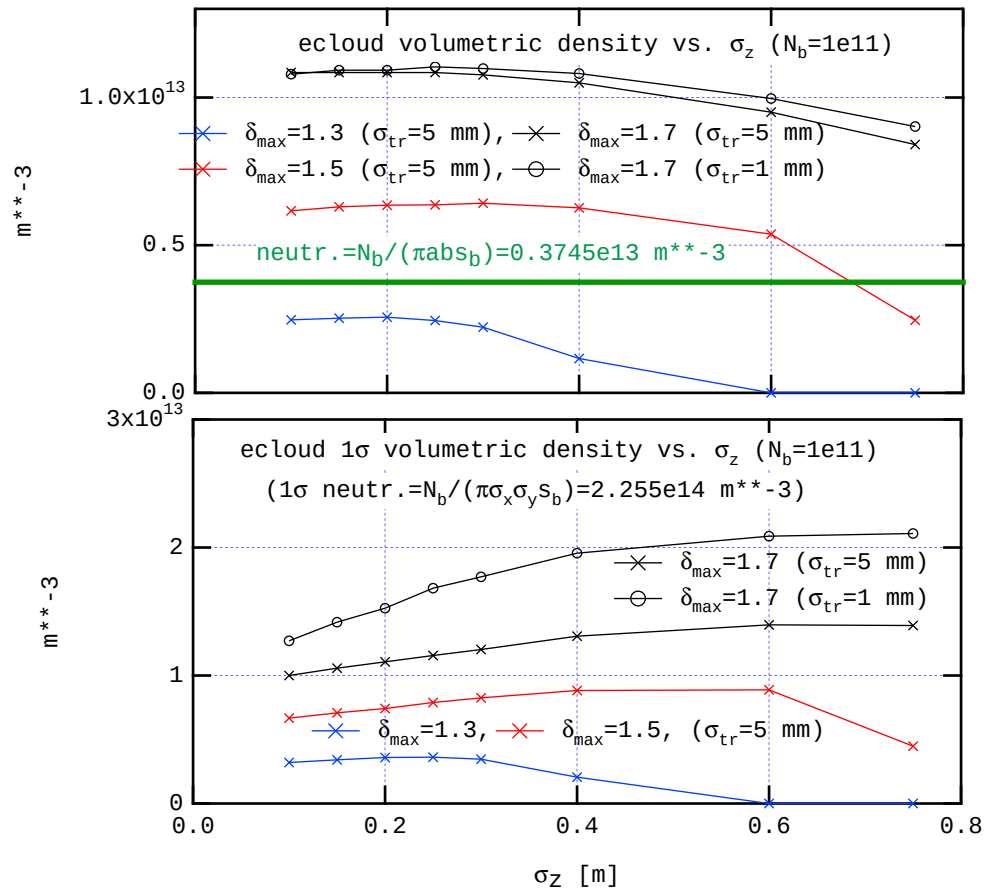

FIG. 5: Bunch-length dependence of the average steady-state density of the electron cloud for $N_b = 1 \times 10^{11}$, for peak SEY $\delta_{\max} = 1.3$, 1.5 or 1.7. Top: overall density in the chamber. Bottom: density within the 1σ cylinder about the beam center. In the top case, the beam neutralization level is given by $d = N_b/(\pi abs_b) = 3.745 \times 10^{12}$ m^{-3}, while in the bottom case the local beam neutralization density is $d = N_b/(\pi\sigma_x\sigma_y s_b) = 2.255 \times 10^{14}$ m^{-3} (assuming $\sigma_x = \sigma_y = 5$ mm). These results imply that, while the overall electron density may exceed the beam neutralization density by factors of 2–3 for high $\delta_{\max}$, the *local* electron density (near the beam) is an order of magnitude below the local neutralization level. For $\delta_{\max} = 1.3$ and 1.5, the RMS transverse beam size $\sigma_{\rm tr}$ is 5 mm, while for $\delta_{\max} = 1.7$, $\sigma_{\rm tr} = 5$ mm or 1 mm ($\sigma_{\rm tr} \equiv \sigma_x = \sigma_y$). The dependence on $\sigma_{\rm tr}$ is strong for the 1σ density, but weak for the overall density.

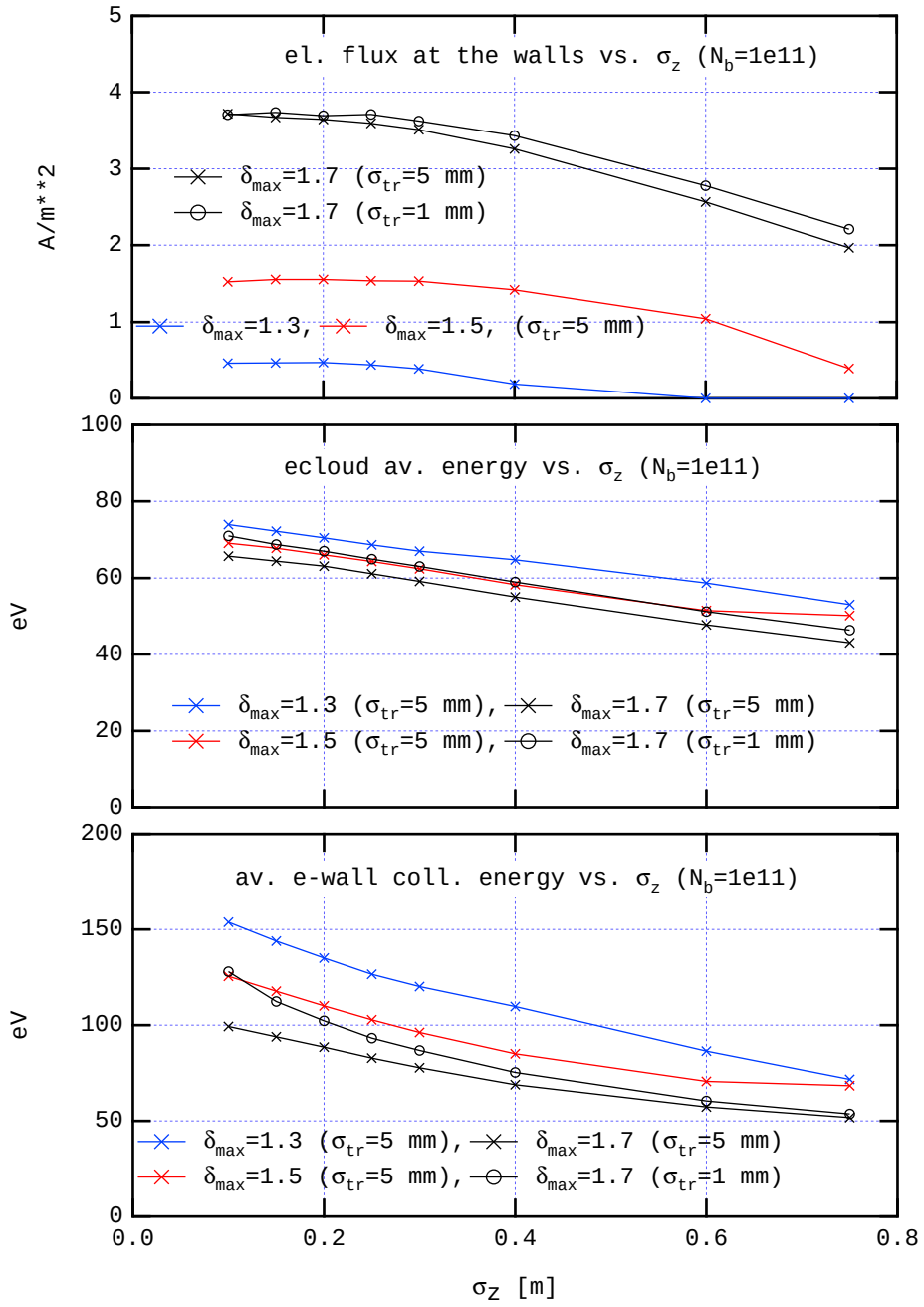

FIG. 6: Bunch-length dependence of the steady-state average incident electron flux at the chamber walls (top), average electron energy in the cloud (middle), and average electron-wall collision energy (bottom), for $\delta_{\max} = 1.3$, 1.5 and 1.7. In all cases the bunch population was $N_b = 1 \times 10^{11}$. For $\delta_{\max} = 1.3$ and 1.5, the RMS transverse beam size $\sigma_{\rm tr}$ is 5 mm, while for $\delta_{\max} = 1.7$, $\sigma_{\rm tr}$ is either 5 mm or 1 mm.

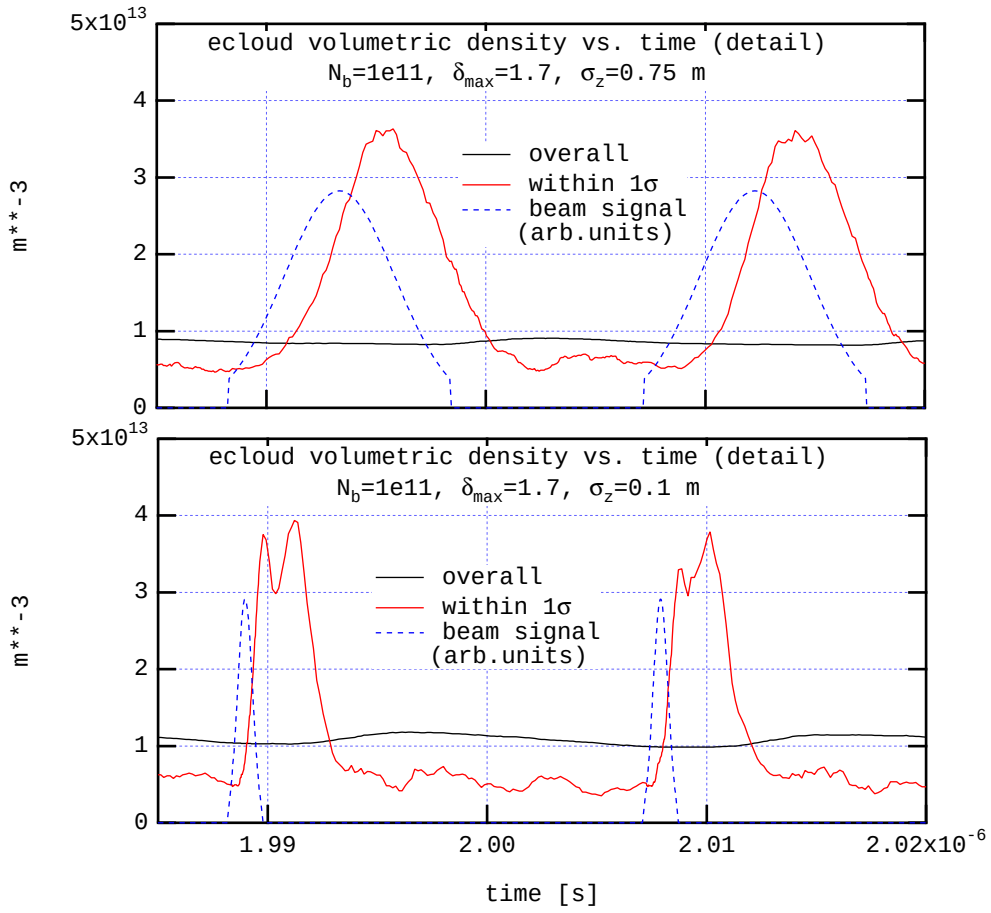

FIG. 7: Average electron-cloud density for $N_b = 1 \times 10^{11}$ and $\delta_{\max} = 1.7$. Top: $\sigma_z = 0.75$ m. Bottom: $\sigma_z = 0.1$ m. These plots show the detail of the time evolution of the density during the passage of two consecutive bunches during a total time interval of 35 ns, after steady state has been reached (see the two bottom plots in Fig. 3). The 1σ density exhibits much stronger fluctuations than the overall density because the bunch strongly pulls in the local electrons, leading to a large electron density gradient along the bunch length. This effect is stronger for the 0.75-m-long bunch than for the 0.1-m-long bunch, implying a larger space-charge neutralization tune shift in the former case than in the latter, and a higher potential for electron-cloud-induced instability.

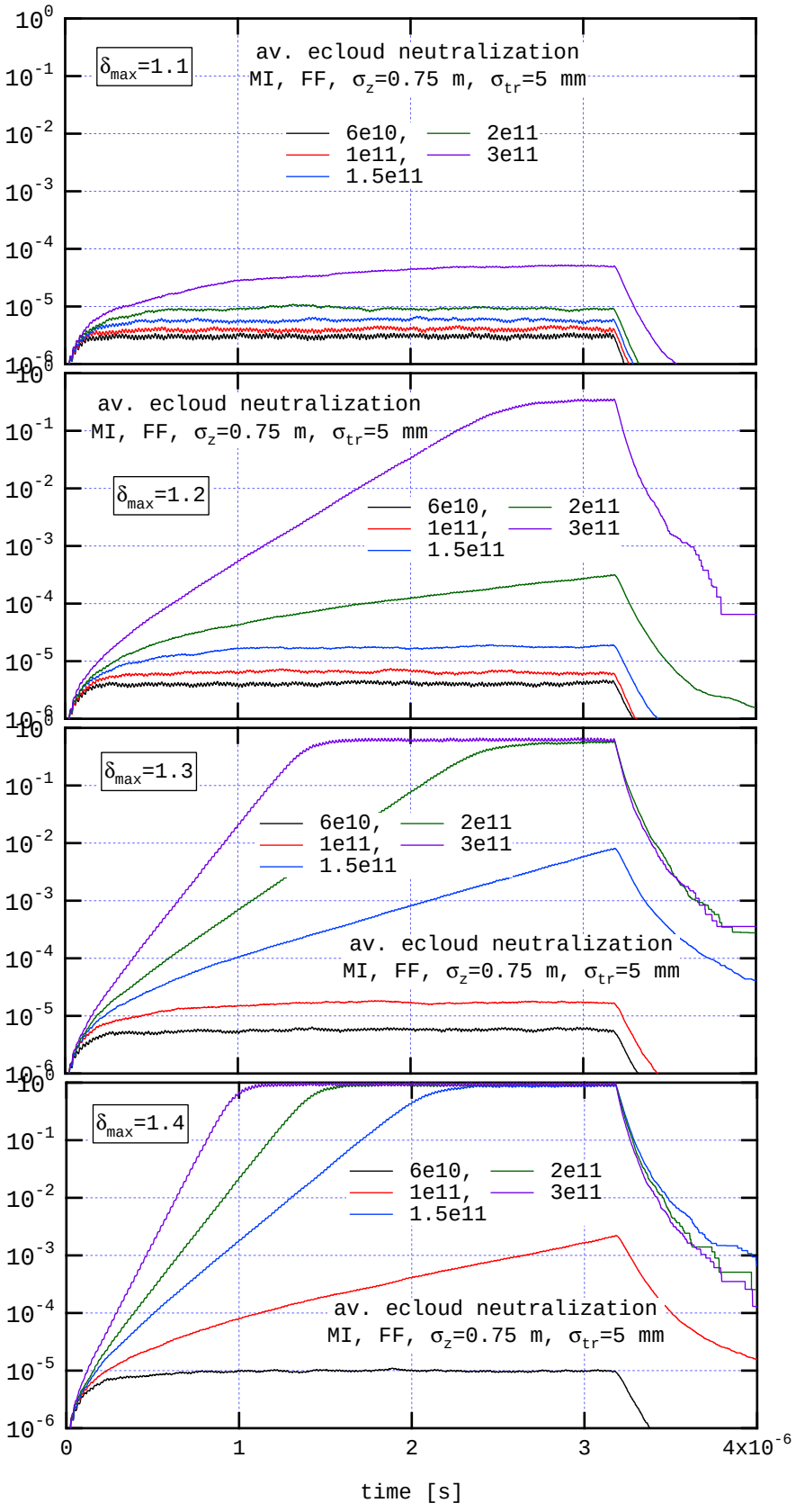

FIG. 8: Build up of the average electron-cloud neutralization factor $\chi(t)$ for $\delta_{\max} = 1.1 - 1.4$ and $N_b = (6 - 30) \times 10^{10}$. $\chi(t)$ is defined as $\lambda_e(t)/\bar{\lambda}_b$, where $\lambda_e(t)$ is the instantaneous electron-cloud line charge density and $\bar{\lambda}_b = eN_b/s_b$. The beam consists of 2 booster batches (168 bunches). Each trace corresponds to a given bunch intensity N_b, as indicated, and each graphic corresponds to a given peak value $\delta_{\max}$ of the SEY, as shown in the box. For all cases, the RMS bunch length was assumed to be $\sigma_z = 0.75$ m and the RMS transverse size to be $\sigma_{\rm tr} = 5$ mm. The exponential growth of the cloud density is clearly exhibited for sufficiently high N_b or $\delta_{\max}$.

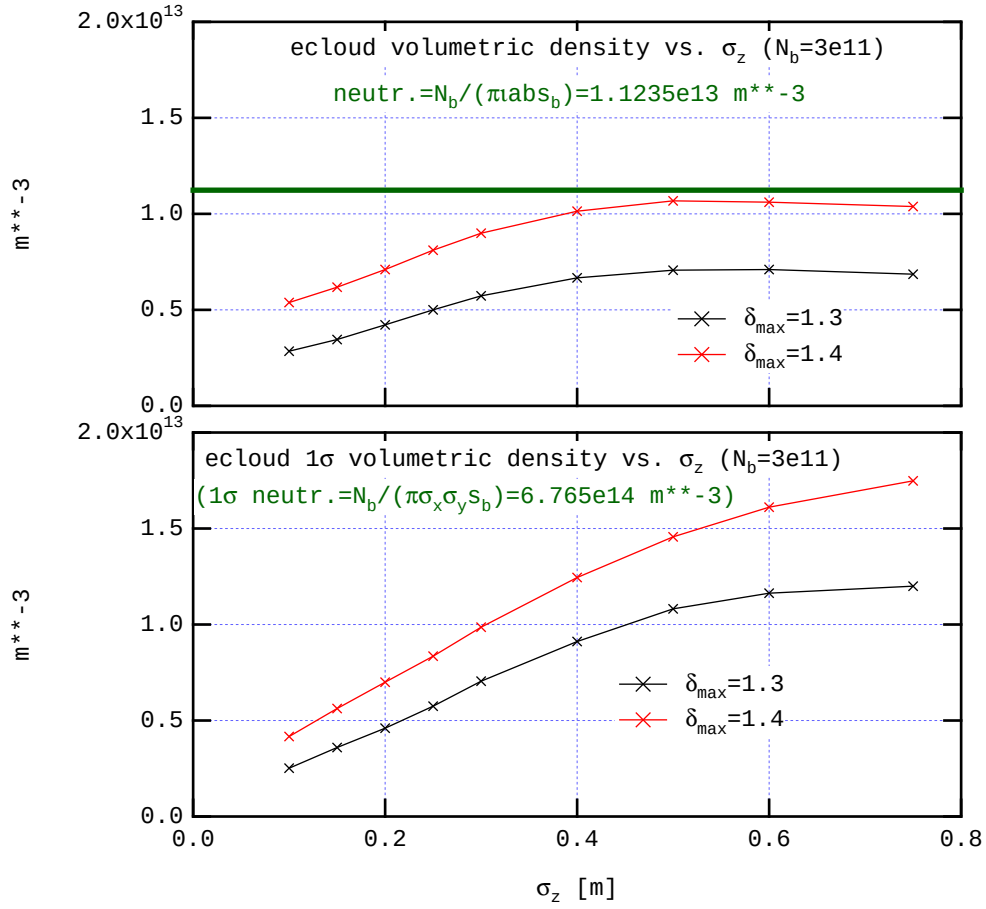

FIG. 9: Bunch-length dependence of the average steady-state density of the electron cloud for $N_b = 3 \times 10^{11}$, for peak SEY $\delta_{\max} = 1.3$ and 1.4. Top: overall density in the chamber. Bottom: density within the 1σ cylinder about the beam center. In the top case, the beam neutralization level is given by $d = N_b/(\pi a b s_b) = 1.1235 \times 10^{13}$ m^{-3}, while in the bottom case the local beam neutralization density is $d = N_b/(\pi\sigma_x\sigma_y s_b) = 6.765 \times 10^{14}$ m^{-3} (assuming $\sigma_x = \sigma_y = 5$ mm).

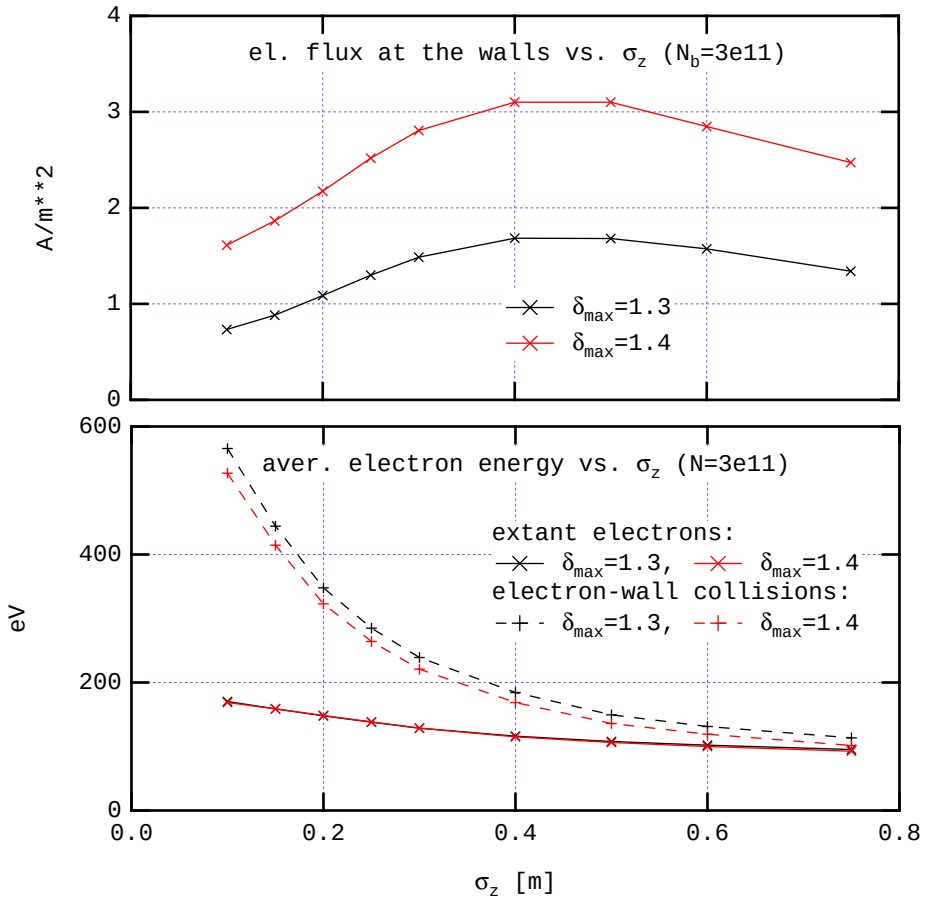

FIG. 10: Bunch-length dependence of the steady-state average incident electron flux at the chamber walls (top), average electron energy in the cloud, and average electron-wall collision energy (bottom), for $\delta_{\max} = 1.3$ and 1.4. In all cases the bunch population was $N_b = 3 \times 10^{11}$ and the transverse RMS beam size was $\sigma_{\rm tr} = 5$ mm.

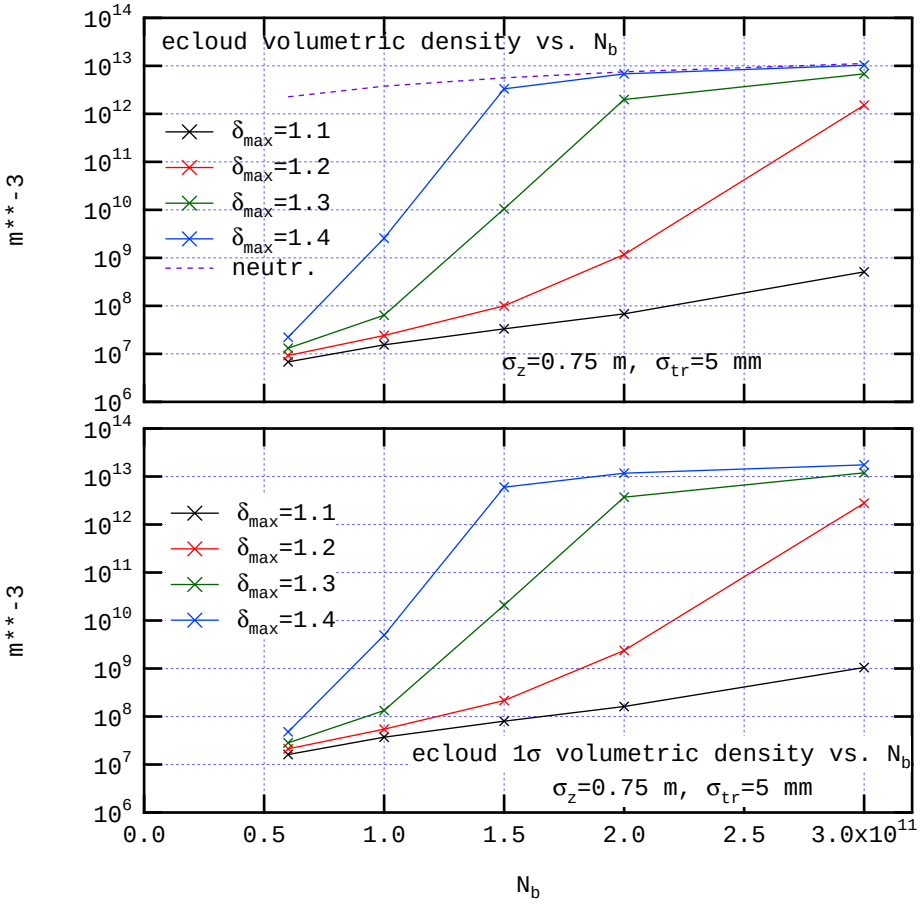

FIG. 11: Bunch-intensity dependence of the average steady-state density of the electron-cloud for $\delta_{\max} = 1.1 - 1.4$. For all cases, the RMS bunch length was assumed to be $\sigma_z = 0.75$ m and the RMS transverse size to be $\sigma_{\rm tr} = 5$ mm. The purple dotted line in the top plot indicates the average beam neutralization level, given by $N_b/(\pi abs_b)$. In the case of the 1σ density, the local beam neutralization level, $N_b/(\pi\sigma_x\sigma_y s_b)$, is off-scale, being 1.353×10^{14} m^{-3} for the lowest value of N_b considered, namely $N_b = 6 \times 10^{10}$.

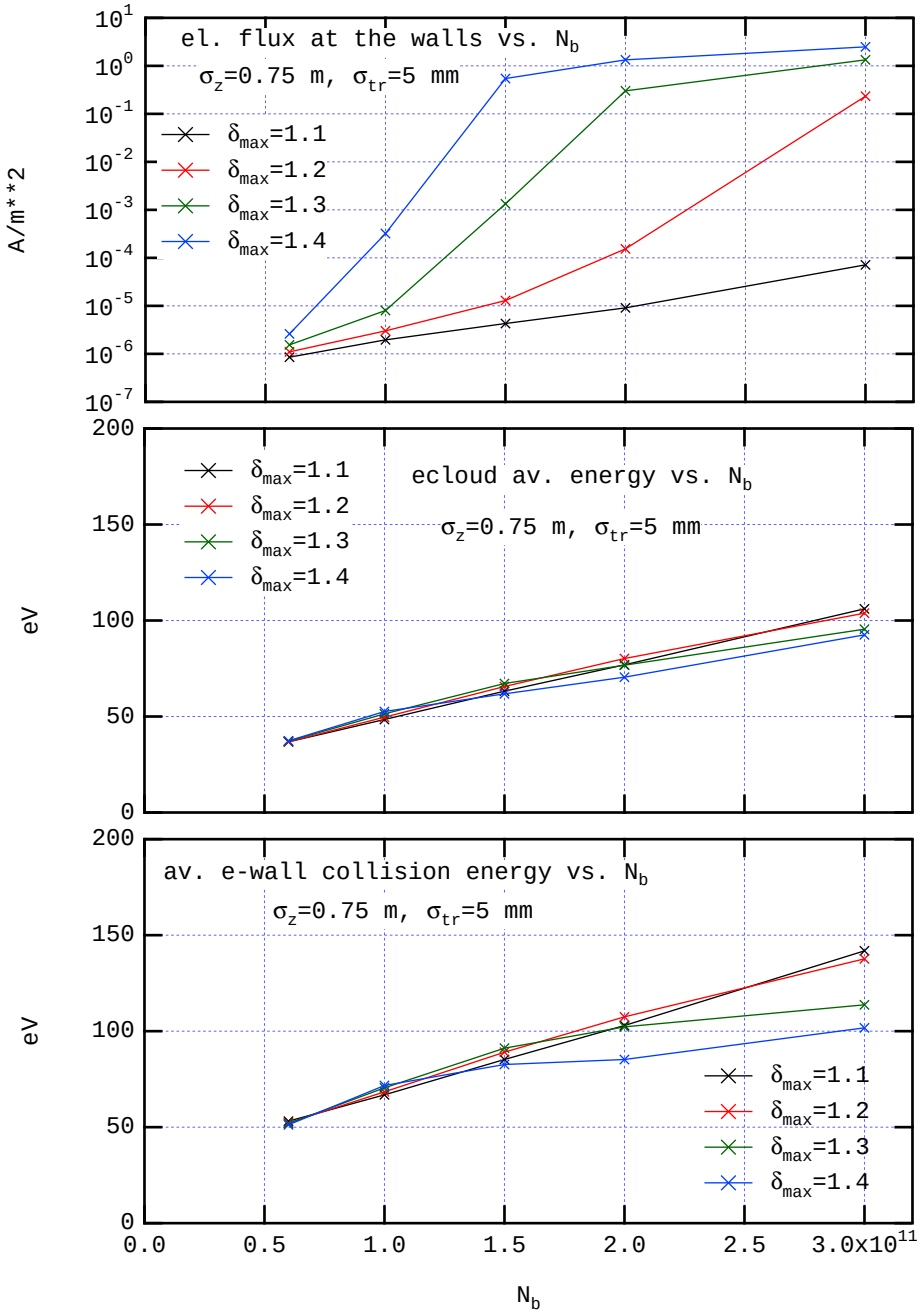

FIG. 12: Bunch-intensity dependence of the steady-state average incident electron flux at the chamber walls (top), average electron energy in the cloud (middle), and average electron-wall collision energy (bottom), for for $\delta_{\max} = 1.1 - 1.4$. In all cases the bunch population was $N_b = 1 \times 10^{11}$. For all cases, the RMS bunch length was assumed to be $\sigma_z = 0.75$ m and the RMS transverse size to be $\sigma_{\rm tr} = 5$ mm.

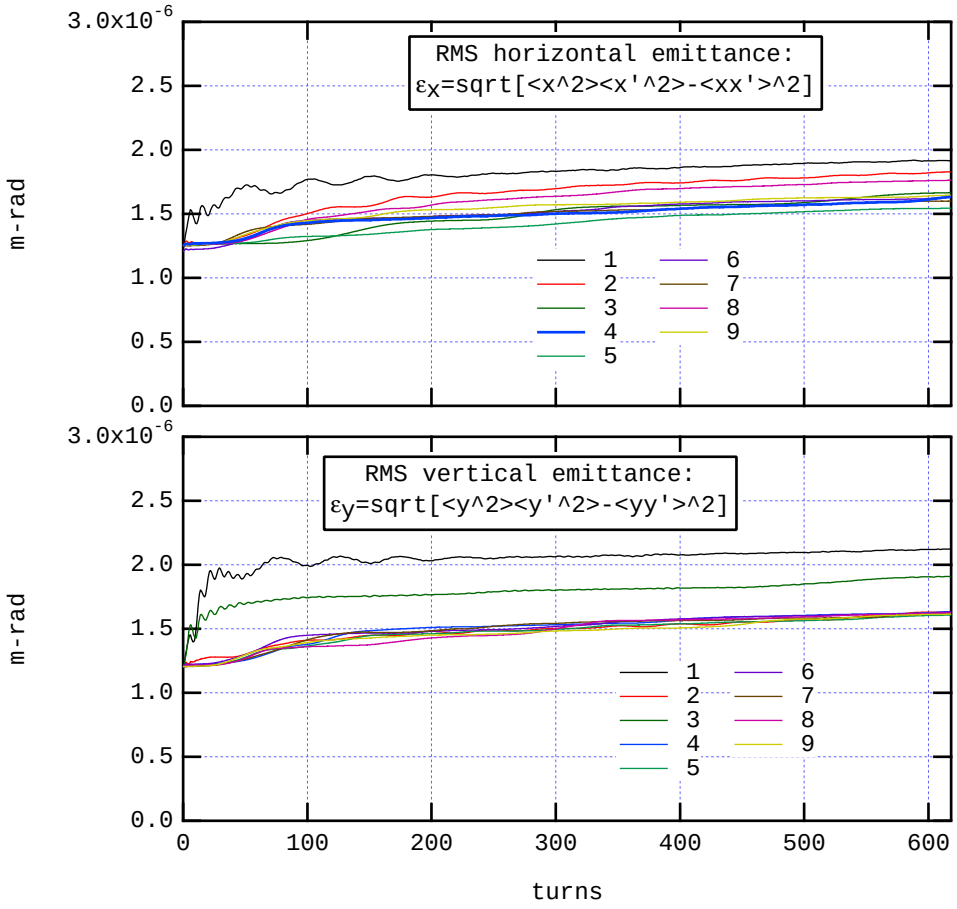

FIG. 13: Time evolution of the beam emittances due to the electron cloud obtained with the code WARP/POSINST in quasi-static mode. The electron cloud was assumed to have an average density of 1×10^{12} m^{-3}, while the bunch was assumed to have $N_b = 3 \times 10^{11}$ and $\sigma_z = 0.75$ m. Any given trace corresponds to the approximation in which the beam-(electron cloud) interaction is lumped at $N_s = 1, 2, \ldots, 9$ points around the ring, as labeled (these locations of beam-(electron cloud) interaction are called "stations"). The lattice was assumed to be linear with tunes $(\nu_x, \nu_y) = (26.425, 25.415)$ and average betas $(\bar{\beta}_x, \bar{\beta}_y) = (20.0, 20.8)$ m. The beam was represented by 3×10^5 macroprotons, and the electron cloud at each station by 1×10^5 macroelectrons.